Check for updates

Short-range nanoregions and nanosized defects in LiFeO$_2$ compound deduced from Mössbauer spectroscopy and Rietveld analysis

V. Panagopoulos[1,2], E. Devlin[1], Y. Sanakis[1], V. Psycharis[1], M. Pissas[1,a)] (ID)

[1] *Institute of Nanoscience and Nanotechnology, NCSR Demokritos, Aghia Paraskevi, 15310 Athens, Greece*
[2] *School of Applied Mathematical and Physical Sciences, National Technical University of Athens, Athens, Greece*
a) Address all correspondence to this author. e-mail: m.pissas@inn.demokritos.gr

We examined the crystal and magnetic properties of the polymorphic LiFeO$_2$ compound using Mössbauer spectra (MS), X-ray diffraction data (XRD), and magnetic measurements. X-ray diffraction analysis of α-LiFeO$_2$ and β'-LiFeO$_2$ phases reveals that short-range ordering observed in the α-LiFeO$_2$ phase is potentially linked to the β'-LiFeO$_2$ phase nanoregions. Low-temperature MS of the α-LiFeO$_2$ phase reveal a complicated disordered magnetic state below 90 K. Rietveld analysis of the XRD data of the γ-LiFeO$_2$ phase reveals a defect microstructure. These defects produce a complicated distribution of the hyperfine magnetic field estimated from MS. While it is not possible to produce the β'-LiFeO$_2$ phase in pure form, extended annealing of the α-LiFeO$_2$ phase at 400 °C yields a nanocomposite material comprising nanoregions of both β'-LiFeO$_2$ and γ-LiFeO$_2$ phases.

Introduction

Ternary oxides LiMO$_2$ (M = Ti, Mn, Fe, Ni, and Co) display interesting crystal and physical properties [1] and can be used in several applications, among the most current being cathodic materials in lithium-ion batteries. The polymorphic LiFeO$_2$ compound has been studied in the past by several researchers [2–13]. Its crystal structure depends on temperature and pressure. At high temperatures 750 °C $\leq T \leq$ 1100°C and ambient pressures, LiFeO$_2$ crystalizes in the cubic NaCl-type structure [4] (space group $Fm\bar{3}m$ (No. 225)). This is the α-LiFeO$_2$ phase. Since this phase is metastable below 700 °C it can be prepared by quenching or slow cooling from high temperatures due to slow kinetics in transforming to more stable forms, γ, β, or β' (see Supplementary information (SI) Fig. S1). This compound has been studied in the past with transmission electron microscopy [6, 14–16] neutron and Mössbauer spectroscopy [4, 17–19]. Moreover, Layek et al. [11] discovered a pressure-induced spin crossover of the Fe ion from high to low spin in α-LiFeO$_2$. Du et al. [19] observed peculiar magnetic ac-susceptibility data in α-LiFeO$_2$ phase, attributing this behavior to iron-rich nano-scale clusters with short-range order.

The earlier neutron diffraction data of Cox et al. [4] revealed that at $T = 4.2$ K, in addition to the diffraction peaks predicted from the cubic α-LiFeO$_2$ crystal structure, broad diffraction peaks with half-integer indices appear, attributed to sort-range magnetic correlations of the Fe^{3+} magnetic moment. These peaks can be interpreted assuming an MnO-type magnetic structure for the iron magnetic moments. To account for the relative intensity of the magnetic Bragg peaks (1/2, 1/2, 1/2) and (3/2, 1/2, 1/2) Cox et al. [4] argued that the spin axis lies within the (111) plane. These broad peaks are present and above 90 K, implying that their origin has to do also with some short-range order. The high-temperature diffuse scattering is also observed in the X-ray [6, 7] and electron diffraction patterns [15, 20], indicating that it may arise from Fe and Li clustering (short-range order). For the β, β', and γ phases, there are only a few studies available [4, 9, 18, 21–23]. Some of them pertain to crystallographic studies of samples prepared using hydrothermal synthesis [18, 21, 22]. The works of Brunel et al. [23] and Famery et al. [9] on single crystal and powder samples attempt to explain the defect structure of these compounds using antiphase structural models. Mössbauer spectra have been published sporadically, for selected temperatures without any direct connection to the X-ray and magnetization data.

As previously noted, apart from the interesting crystal chemistry properties of the LiFeO$_2$ compound, these lithium double oxides may also prove to be useful in lithium battery technology. Hu et al. [24] demonstrated that nanosized α-LiFeO$_2$ can be a cathode material with excellent electrochemical performance. Zhang et al. [25] found that a polypyrrole coating to α-LiFeO$_2$ nanoparticles enhanced their capacity and cycling stability in lithium batteries. It was found [26, 27] that nanosized α-LiFeO$_2$ electrodes provide good capacity during the first cycles and show adequate cycling life. Rahman et al. [12] found that a thin carbon layer on a nanosized α-LiFeO$_2$ anode electrode enhances capacity and cycle stability. Morales et al. [28] studied α-LiFeO$_2$ electrodes during cycling, and they confirmed that Fe ions change valence during this procedure and that after the first cycle, a layer of solid electrolyte interface begins to form. With α-LiFeO$_2$ as the cathode material, a 150 mAh/g stabilized capacity is achievable. Hirayama et al. [29] found that reducing the particle size and disorder in the cation layers enhances the electrochemical activity of LiFeO$_2$ particles. Lee et al. [30] observed that an orthorhombic form of LiFeO$_2$ collapses into the spinel structure during cycling, with a significant impact on capacity. Wu et al. [31] found that there are no structural changes to the cubic lattice during cycling. Suresh et al. [32] found support that the solution-combustion production of LiFeO$_2$ leads to enhanced initial capacity. The γ-LiFeO$_2$ phase has also been studied electrochemically as an anode material for lithium-ion batteries [33].

Here, we present a detailed crystallographic and Mössbauer study of three of the polymorphic phases of the LiFeO$_2$ compound, prepared by solid-state reaction of Li$_2$CO$_3$ and Fe$_2$O$_3$ reagents in an air atmosphere. We also use magnetic measurements to study the magnetic properties and the magnetic transitions. Our MS, specific heat and magnetization data indicate that the α-LiFeO$_2$ exhibit a disordered magnetic state below 90 K. The γ-LiFeO$_2$ phase is produced in pure form after prolonged annealing at 600 °C for 30 days. Fitting of the MS and Rietveld analysis shows that in this phase, extended defects, possible anti-phase domains (inherent to the ordering structural transition) produce selective broadening of the XRD Bragg peaks and a distribution of the magnetic effective hyperfine magnetic fields seen by iron nuclei. The β'-LiFeO$_2$ phase cannot be produced as a single-phase material. Prolonged annealing of the α-LiFeO$_2$ phase at 400 °C produces a nanocomposite material consisting of nanoregions of β'-LiFeO$_2$ and γ-LiFeO$_2$ phases. A small amount ($\approx 5\%$) of α-LiFeO$_2$ phase remains untransformed. From the time evolution of the α-LiFeO$_2$ phase at 400 °C, we can conclude that the short-range ordering observed in the α-LiFeO$_2$ phase is related to nanoregions of the β'-LiFeO$_2$ phase.

Rietveld analysis of the X-ray diffraction data

X-ray diffraction data of α-LiFeO$_2$ phase

The x-ray diffraction data of of α-LiFeO$_2$ phase were analyzed with the Rietveld method (see SI Fig. S2 for the Rietveld plot). The Bragg peaks are described with a pseudo-Voigt function (#7, see FullProf user guide [34]). The angular dependence of the full width at the half maximum (FWHM) of the Gaussian and Lorentzian parts are given by the formulas $\Gamma_G^2 = U\tan^2\theta + V\tan\theta + W + IG/\cos^2\theta$ and $\Gamma_L = X\tan\theta + Y/\cos\theta$, respectively. The instrumental FWHM parameters are estimated using the NIST 640C standard LiB$_6$ sample. The parameters reported here represent the additional broadening with respect to the LiB$_6$ sample. Only the X, Y parameters are refined. The others were held to be zero, ($W = U = V = IG = 0$). We refine the crystal structure (see SI Fig. S1 (upper panel)) with a cubic face-centered space group $Fm\bar{3}m$. In that case, the only structural parameters are the cell constants, the relative occupancy of Li and Fe at the $4a$, $(0, 0, 0)$ (site symmetry $m\bar{3}m$) and the thermal parameters. The estimated cell constant is found to be $a = 4.159(1)$Å and the relative occupancy ratio of Li:Fe was estimated to be nearly 1:1, within the standard deviations (5% for iron and 10% for lithium). The Lorentzian isotropic strain parameter $X = 0.017(1)$ deg., and the Lorentzian isotropic size parameter $Y \approx 0$ (giving a resolution limited apparent size $\langle D \rangle \sim 1\mu$m). The refinement converged, giving profile, weight profile, and Bragg factors: $R_p = 6\%$, $R_{wp} = 7\%$, and $R_B = 4.8\%$, respectively. By a close inspection of the background, one can see significant diffuse scattering around 20°, 30° and 60°. The intensity around 30° arises mainly from the glass sample holder. Similar diffuse scattering has been observed in the neutron diffraction data of Cox et al. [4]. As we see below, the diffuse scattering may be related to the $\beta' - $ LiFeO$_2$ nanoregions.

X-ray diffraction data of γ-LiFeO$_2$ phase

Figure 1 shows the Rietveld plot of the refined XRD data of the γ-LiFeO$_2$ phase. γ-LiFeO$_2$ is a tetragonal distorted superstructure form of the α-LiFeO$_2$ compound with (see SI, Fig. S1 (middle panel)) $a_t < a_c, c_t > 2a_c$, where a_t, c_t, a_c are the cell constants of the tetragonal and cubic phase, respectively. The crystal structure was refined using the space group $I4_1/amd$ (No. 141). The Li and Fe cations occupy the special positions $4b$ and $4a$ with coordinates $(0, 1/4, 3/8)$ and $(0, 3/4, 1/8)$, respectively, both with point symmetry $- 4m2$. The oxygen anions occupy the special position $8e$ $(0, 1/4, z)$. The Rietveld method was applied to the XRD measurements of the γ-LiFeO$_2$ compound, adopting the following strategy. Similar to the α phase case, we set $U = V = IG = 0$ and $W = 0$. During the refinement, the global
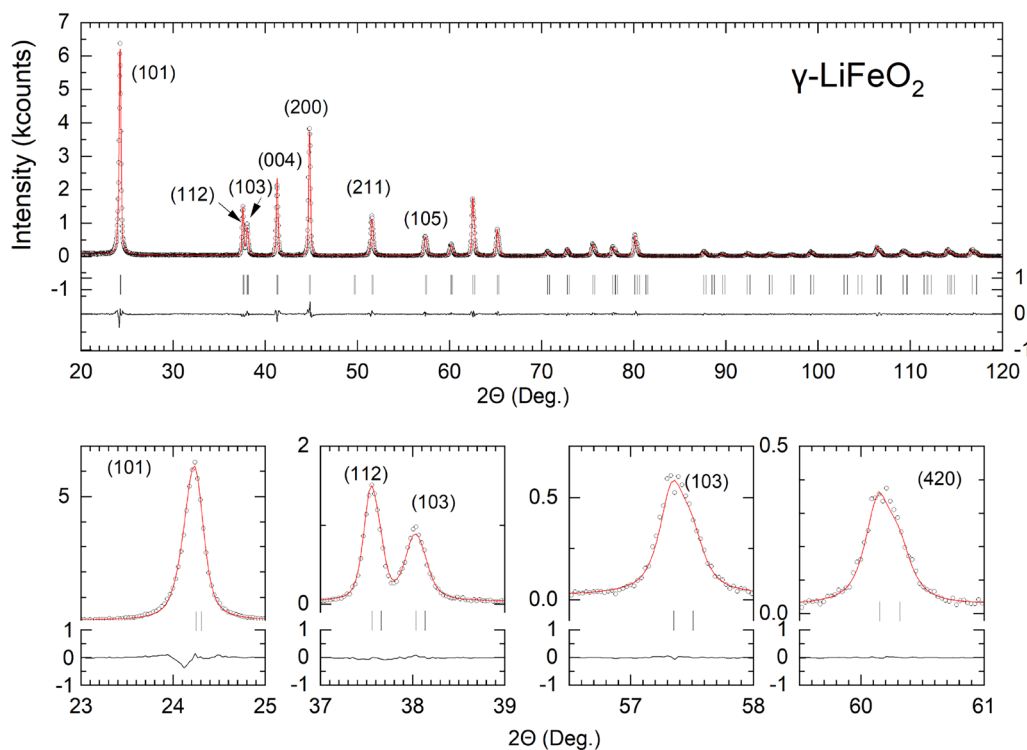
Figure 1: (Upper panel) Rietveld plot of γ-LiFeO$_2$ phase. The open dots correspond to the experimental X-ray diffraction pattern. The red solid line is the theoretical x-ray diffraction pattern, calculated from the structural and microstructural parameters. The short vertical lines indicate the position of the expected Bragg peaks. The black solid line represents the difference between the experimental and theoretical calculated patterns. The lower panel shows Rietveld plots of selected reflections.

strain and size parameters X, Y, respectively, are left free to vary. The free parameters in the refinement were the cell parameters, the oxygen z coordinate, the Li, Fe, and O temperature factors, and the Fe and Li relative occupancy in the special positions $4a$ and $4b$. With this model, the refinement converged, giving the following agreement parameters $R_p = 11.8\%$, $R_{wp} = 16.1\%$, $R_B = 3.85\%$. Although the obtained R_B has an acceptable value, the profile agreement factors R_p, R_{wp} are rather high.

By close inspection of the refined X-ray diffraction patterns, we find that several peaks, mainly describing the ordering of lithium and iron ions, are broader than in comparison to those of the disordered state. This selective broadening observed in the Bragg peaks with $\ell = 2n + 1$ (arising from Li/Fe ordering) leads us to model these peaks with a different size parameter (IsizeModel$= -1$, see Fullprof user guide [34], p. 22), significantly improving the Rietveld agreement parameters. Convergence was achieved with the following agreement parameters $R_p = 8.9$, $R_{wp} = 13.2$, $\chi^2 = 1.84$ and $R_B = 2.46$. These parameters yielding the χ^2 minimum are: $a = 4.0469(1)$Å, $c = 8.7489(1)$Å, $z(O) = 0.1052(2)$, $o(4a) = 0.247(\text{Li}) + 0.003(\text{Fe})$, $o(4b) = 0.247(\text{Fe}) + 0.003(\text{Li})$, $B(\text{Li}) = 1.4(3)$Å^2, $B(\text{Fe}) = 0.31(2)$Å^2, $B(\text{O}) = 0.27(5)$Å^2, $X = 0.085(4)$ (deg.), $Y = 0.029(2)$ (deg.) and Lorentzian size parameter, for Bragg peaks with $\ell = 2n + 1$, equal to 1.31(3). The significant finding from the

Rietveld refinement is that the lithium and iron ions occupy the special positions $4b$ and $4a$, respectively. The bond lengths and bond valence sums of the ferric iron and lithium ions, which are octahedrally coordinated with oxygen ions, are estimated to be Li–O = 2.360(3)Å × 2, Li–O = 2.0308(2)Å × 4, $BVS = 0.881(1)$ and Fe–O = 2.015(3)Å × 2, Fe–O = 2.0308(2)Å × 4, $BVS = 2.961(5)$, respectively. The Fe–O bond lengths exhibit minimal variation for iron, leading to an approximately regular octahedron. In contrast, for lithium, two out of the six Li–O bond lengths are greater than the remaining four, resulting in an elongated octahedron. The bond valence sums closely approach the ideal values of 1 for Li^{1+} and 3 for Fe^{3+}. The refined crystal structure results obtained at this stage agree well with neutron data from samples prepared using solid-state reaction and hydrothermal synthesis methods [4, 18, 21].

Let us next discuss what information on the microstructure can be obtained from the selective broadening of the Bragg peaks. Figure 2 illustrates the Williamson–Hall (WH) diagram [35] constructed using FWHM parameters, which describe both the average and superstructure Bragg peaks ($\ell = 2n + 1$). In this diagram, we plot the effective FWHM parameter $\beta_{hk\ell}^* = \beta_{hk\ell} \sin\theta / \lambda$ versus the inverse distance $d_{hk\ell}^* = 1/d_{hk\ell}$ for all the Bragg peaks. The points on the WH diagram are categorized into two groups with distinct size
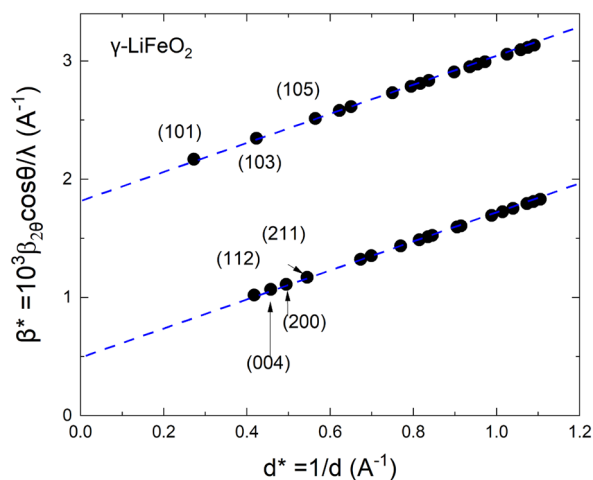
Figure 2: Williamson–Hall plot of γ-LiFeO$_2$ phase.

parameters characteristic of the superstructure and the peaks associated with the disordered structure. According to the WH relation $\beta^* = 2\epsilon d^* + 1/\langle L \rangle$, the data points should lie on two straight lines. The intersections of these lines with the y-axis yield an estimation of the inverse average crystalline size, while the slope provides the 2ϵ parameter which is related to strain. As the two categories of peaks possess distinct size parameters, the Williamson–Hall graph is expected to exhibit two parallel lines, as it does. From the slope of the lines, we calculate the maximum strain [36] parameter $\epsilon = 5.88(4) \times 10^{-4}$. Furthermore, the y-axis intersection points allow an estimate of the average crystalline size for both categories of Bragg peaks. Specifically, the average size of the diffraction domains associated with the Li/Fe ordering measures $\langle L \rangle = 54$ nm, while the average size deduced from the Bragg peaks of the disordered structure $\langle L \rangle = 188$ nm. This microstructure nay result from antiphase domains.

The differential temperature analysis (DTA) measurements versus temperature (see SI, Fig. S2) for the γ-LiFeO$_2$ phase show on heating, a clear endothermic peak is observed with onset temperature $T_{on} = 687$ °C and local minimum temperature $T_{min} = 709$ °C. This negative peak is related to the endothermic structural transformation from the ordered to the disordered state (γ-LiFeO$_2 \rightarrow \alpha$-LiFeO$_2$). The area of the endothermic negative peak represents the latent heat that must be absorbed by γ-LiFeO$_2$ (ordered state) to be transformed into α-LiFeO$_2$ (disordered state). While cooling, one may expect an exothermic peak due to the anticipated transition from a disordered to an ordered state. However, the kinetics of this structural transformation are very slow (in comparison to the time needed to cool the sample in the DTA apparatus, a few hours), which does not allow the α to γ phase transformation at this specific cooling rate.
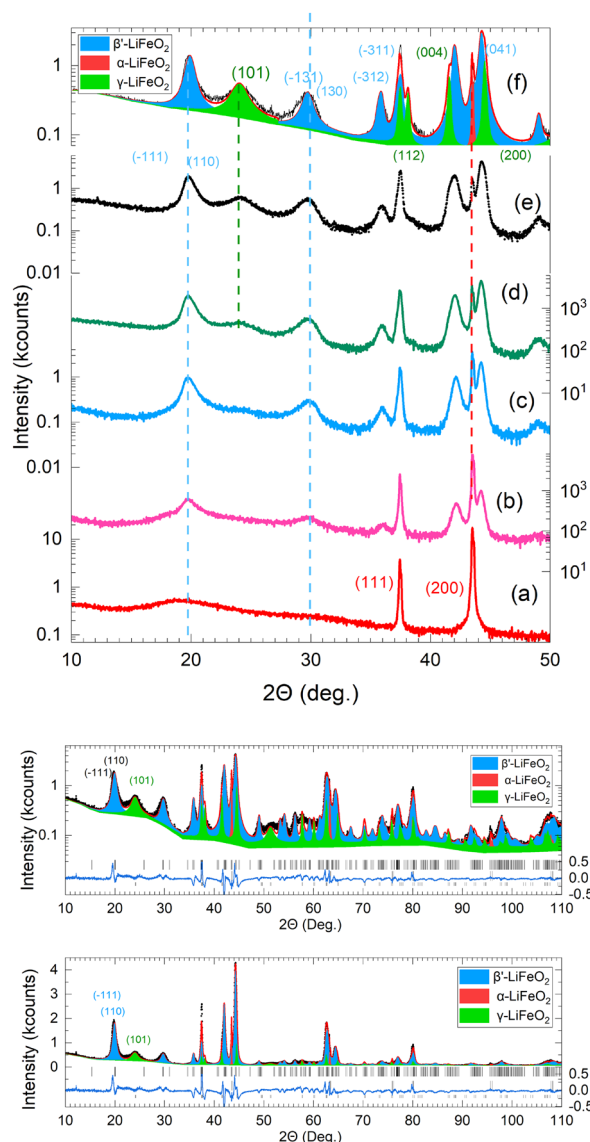

Figure 3: (Panels a–f) Evolution with annealing time at ~ 400 °C for 37 days of the XRD patterns of a sample which initial has the α-LiFeO$_2$ structure. The panels (a)–(f) display the powder XRD patterns after 3, 10, 16, 23, 30, and 37 days of annealing, respectively. (lower panel) Rietveld plot of LiFeO$_2$, sample annealed at 400 °C for a month. In the lower panel, the intensity scale is linear, whereas in the upper panel is logarithmic.

X-ray diffraction data of the nominal β' LiFeO$_2$ sample

Despite using various heating protocols, we were unable to successfully synthesize the β'-LiFeO$_2$ phase in pure form through a solid-state reaction in an air atmosphere. Figure 3 illustrates the time evolution of the XRD patterns from our attempts to prepare the β'-LiFeO$_2$ phase.

Initially, we began with a sample containing only α-LiFeO$_2$ phase. As the annealing time increased part of α-LiFeO$_2$ phase transforms into the β'-LiFeO$_2$ phase (see panels (a)–(c) of Fig. 3).

It is interesting to note that at the locations where diffuse scattering is observed in the XRD data of the α-LiFeO$_2$ phase, the low-angle Bragg peaks of the β'-LiFeO$_2$ phase develop. Therefore, it is reasonable to relate the diffuse scattering observed in the α-phase to β''-phase nanodomains. Furthermore, for more extended annealing periods, the XRD patterns show that the weight percentage of the γ-LiFeO$_2$ phase tends to increase, whereas the amount of α-LiFeO$_2$ phase is reduced by about 5% (for an annealing period of 30 days). It is known that the pure β'-LiFeO$_2$ phase can only be prepared using hydrothermal synthesis methods [21, 22].

Figure 3 (lower panel) shows the Rietveld plots of the sample annealed for 30 days at 400 °C. The Rietveld refinement is performed using a three-phase model, consisting of α-LiFeO$_2$, β'-LiFeO$_2$, and γ-LiFeO$_2$ phases. By employing the structural models of the γ-LiFeO$_2$ and α-LiFeO$_2$ phases ("X-ray diffraction data of α-LiFeO$_2$ phase" and "X-ray diffraction data of γ-LiFeO$_2$ phase" sections), as well as the structural model of the β'-LiFeO$_2$ phase reported by Barre and Catti [21], and applying the same methodology used in the case of the γ-LiFeO$_2$ phase to address the selective broadening (see "X-ray diffraction data of γ-LiFeO$_2$ phase" section), we were able to reproduce the experimental XRD patterns satisfactorily. The estimated weight percentages for the three LiFeO$_2$ phases are 54% for β', 41% for γ and 5% for α. The estimated cell constants for the three phases are as follows: $a = 4.1570(1)$Å for the cubic α-LiFeO$_2$ phase, $a = 4.071(1)$Å and $c = 8.657(2)$Å for the tetragonal γ-LiFeO$_2$ phase, and $a = 8.581(1)$Å, $b = 11.561(2)$Å, $c = 5.202(1)$Å and $\beta = 146.13(1)°$ for the monoclinic β'-LiFeO$_2$ phase. The diffraction peaks of the β' phase with $k = 2n + 1$ display selective broadening. The size parameter for these Bragg peaks was estimated as $SP = 10(1)$, whereas the Lorentzian size parameter for the remaining Bragg peaks was estimated as $Y = 0.26(1)$. These values correspond to diffraction domain sizes of approximately 6.1 nm and 21 nm, respectively. Here, the reflections of the γ phase display severe selective broadening, especially those with $\ell = 2n + 1$. The size parameter estimated through Rietveld refinement for the Bragg peaks with $\ell = 2n + 1$ was $SP = 26(1)$, corresponding to a diffraction domain size of about 3(1) nm. The Lorentzian size parameter for the Bragg peaks with $\ell \neq 2n + 1$ was estimated to be $Y = 0.23(1)$, indicating a domain size of 24(1) nm. What is interesting here is that both β'-LiFeO$_2$ and γ-LiFeO$_2$ phases show a severe broadening of the diffraction peaks, indicating that these phases consist of nanoregions possible within the original crystallites of the α-LiFeO$_2$ phase. In practice, the prolonged annealing of the α-LiFeO$_2$ phase at this temperature produces a nanocomposite material via a metastable phase. It is important to emphasize that the remaining small amount of α-LiFeO$_2$ phase has narrow diffraction peaks. The phase identification mentioned above is based only on Rietveld analysis of the powder XRD patterns. The knowledge of

the XRD pattern of the α-phase and the XRD patterns observed during the α to γ transformation it leaves little doubt about the correctness of our model. However, future electron transmission diffraction data may also provide an additional check about the phase indication and the spatial arrangement of the observed nanophases.

Mössbauer spectra

α-LiFeO$_2$

Figure 4 shows the paramagnetic Mössbauer spectra of the α-LiFeO$_2$ compound, measured at $T = 290$ K. The spectrum consists of a symmetric, doublet, with half-width at half maximum (HWHM, $\Gamma/2$) larger than the instrumental minimum of our spectrometer ($\Gamma/2 \approx 0.14$ mm/s).

An initial attempt to fit the spectra with only one doublet ($\Gamma/2 = 0.3$ mm/s, $\delta = 0.4$ mm/s, and $\Delta E_Q = 0.7$ mm/s) was unsatisfactory. By adding a second doublet, the fitting results were significantly improved. The estimated hyperfine parameters for the two-site model are: $\Gamma_1/2 = 0.18$ mm/s, $\delta_1 = 0.38(1)$ mm/s, $\Delta E_{Q,1} = 0.48(1)$ mm/s, $\Gamma_2/2 = 0.17(1)$ mm/s, $\delta_2 = 0.38(1)$ mm/s, and $\Delta E_{Q,2} = 0.87(1)$ mm/s. The relative spectral areas of the two components were found to be $A_1 : A_2 = 63 : 37$. Similar paramagnetic spectra were observed in previous studies [4, 17].

The fitting result can be significantly improved if we assume a continuous distribution of the ΔE_Q values. This task can be accomplished with the help of the Le Caer–Dubois method [37]. In this method, if some hyperfine parameter, denoted as $x = H, \Delta E_Q$, is randomly distributed and can be described by a probability density function, it can be determined by minimizing the following quantity:

$$\tilde{\chi}^2 = \chi^2 + \lambda \int_0^\infty \left(\frac{d^2 p(x)}{dx^2} \right)^2 dx, \qquad (1)$$

where λ is the smoothing parameter, $\chi^2 = \sum_{i=1}^N w_i (Y_e(i) - Y(i))^2$ (the classical Chi-squared statistic), and $Y_e(i)$, $Y(i)$ represent the experimental and theoretical relative absorptions in the i-channel.

The shape of the calculated distribution depends on the smoothing parameter and the FWHM (Γ). To avoid introducing artificial peaks and features in the ΔE_Q-distribution, we have chosen (using trial end error methodology, see [37]) $\lambda = 85$ and $\Gamma/2 = 0.14$ mm/s as the values for the smoothing parameter and the HWHM, respectively. The isomer shift was estimated from the centroid of the MS. The value which gives the minimum $\tilde{\chi}^2 = 504$ is estimated $\delta = 0.38$ mm/s in perfect agreement with the earlier, simpler, two-component model. This value of the isomer shift indicates high spin ferric iron in an octahedral environment comprising oxygen atoms [38]. The isomer shift value also agrees very well
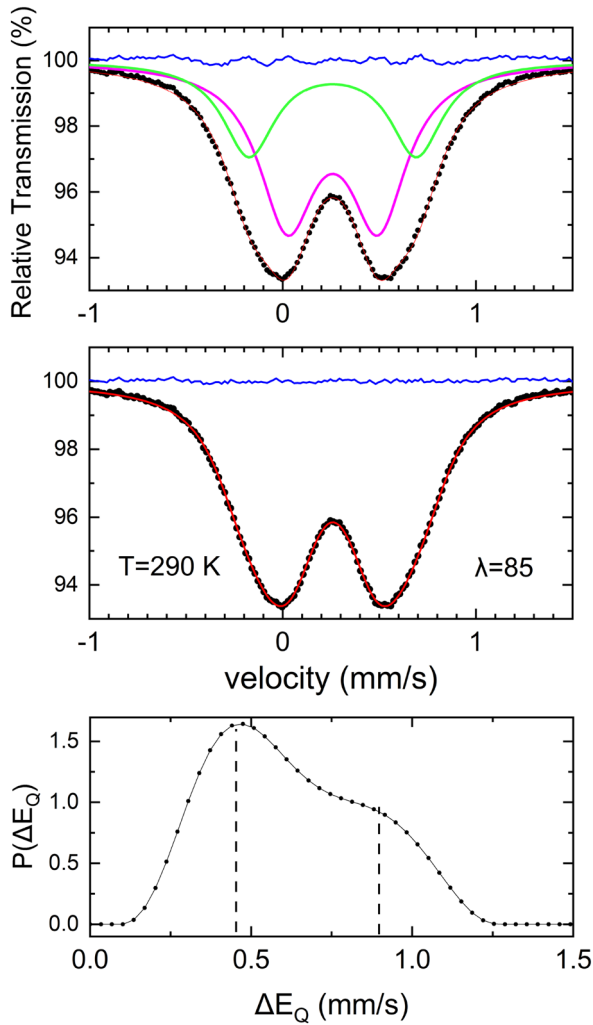
Figure 4: (upper panel) Experimental Mössbauer spectrum (points) of α-LiFeO$_2$, compound at $T = 290$ K. The red solid line represents the theoretical spectrum, calculated with the hyperfine parameters obtained by least squares fitting using two doublets depicted with green and magenta colored solid lines. The (middle panel) shows the same spectrum as the upper panel. The theoretical spectrum (red solid line) is calculated using the quadrupole splitting distribution (see lower panel) estimated with the Le Caer–Dubois method. The blue lines represent the difference between the experimental and theoretical calculated spectra.

with values estimated by Knop et al. [17] (0.364(8) mm/s), Tabuchi et al. [18] (0.37 mm/s), Cox et al. [4] (graphical estimation 0.381 mm/s) and Du et al. [19] (0.37 mm/s doublet I and 0.36 mm/s doublet II). The fitted spectrum and the extracted distribution are shown in Fig. 4 (middle and lower panels). Importantly, the salient features of the estimated $p(\Delta E_Q)$ distribution, including peaks and shoulders, can be directly associated with the two components utilized in the simplified model. The non-zero value of ΔE_Q and, more importantly, the existence of at least two zones in the distribution of ΔE_Q is an interesting finding. The α-LiFeO$_2$ phase crystallizes in the cubic crystallographic system, where iron ions occupy the sites with point group symmetry $m\bar{3}m$. A zero average

$\langle \Delta E_Q \rangle = 0$ is expected. The peculiarities of the ΔE_Q distribution (or the two doublet model used to fit the MS spectra) imply that some short-range order exists in the α-LiFeO$_2$ phase. The Mössbauer spectra from room temperature to $T = 95$ K remain paramagnetic without significant changes. Only the isomer shift, and the area slightly increase as the temperature decreases.

Below $T = 90$ K, the spectra further broaden, indicating the onset of a magnetic transition. As the temperature decreases, the splitting of the absorption Mössbauer lines increases while their broadening decreases (see Fig. 5). At $T = 4.2$ K, a well-defined sextet is observed, albeit with noticeable line broadening. Additionally, the asymmetry in the shapes of lines 1 and 6, combined with the narrow width of lines 3 and 4, reveals that the spectrum consists of at least two components (two sextets). The spectrum cannot be satisfactorily fitted without using two distinct quadrupole shift values, in agreement with the earlier finding of distinct quadrupole splitting values at higher temperatures. Thus, the magnetic MS are fitted with two sextets with distributions of quadrupole shift (u) and hyperfine magnetic field (H). To avoid over-parametrization of the fitting procedure, we have used a constrained model by supposing that the two components have the same half-width at the half maximum ($\Gamma_1/2 = \Gamma_2/2$) and the same isomer shift ($\delta_1 = \delta_2$). Considering the quadrupole interaction as a first-order perturbation, the velocities of the six absorption lines are given from the relations (in velocity units) $v_i = \gamma_i H + \beta_i u + \delta$, where $\beta_1 = \beta_6 = 1$, $\beta_2 = \beta_3 = \beta_4 = \beta_5 = -1$, $\gamma_1 = -\gamma_6 = -0.016035$ (mm/s)/(kG), $\gamma_2 = -\gamma_5 = -0.00928$ (mm/s)/(kG), and $\gamma_3 = -\gamma_4 = -0.002535$ (mm/s)/(kG). The parameter u represents the first-order correction of the excited nuclear levels and is given by the formula: $u = (3/2)[3\cos\theta^2 - 1 + \eta\sin\theta^2\cos 2\phi](e^2Qq/12)$, where θ and ϕ are the polar angles of the H to the principal axes of the EFG tensor of the ^{57}Fe nucleus. In addition, the MS are convoluted with a symmetric Gaussian distribution of the u parameter, $p(u) = 1/(\sqrt{2\pi}\sigma_u)\exp[(u - \bar{u})^2/2\sigma_u^2]$, and an asymmetric distribution of the H,

$$p(H) = \frac{2/\sqrt{2\pi}}{\sigma_l + \sigma_h} \begin{cases} e^{-(H-\bar{H})^2/2\sigma_l^2}, \text{ for } H \leq \bar{H} \\ e^{-(H-\bar{H})^2/2\sigma_h^2}, \text{ for } H \geq \bar{H} \end{cases} \quad (2)$$

for each site. Practically, H takes values within a finite interval. Therefore, in the fitting routine, a truncated asymmetric distribution of H has been implemented, where the magnetic field is restricted to a specific range (0 or $\bar{H} - n_l\sigma_l \leq H \leq \bar{H} + n_h\sigma_h$), with n_h and n_l both equal to 5. The parameters $\bar{u}$ and σ_u represent the mean and standard deviation of the variable u, respectively. Similarly, $\bar{H}$, σ_l, and σ_h represent respectively the mean, low-field, and high-field standard deviations of the variable H. The left panel of Fig. 5 shows the experimental MS together with two sextets, which the hyperfine parameters give the lower χ^2. The right panel depicts the hyperfine field distributions
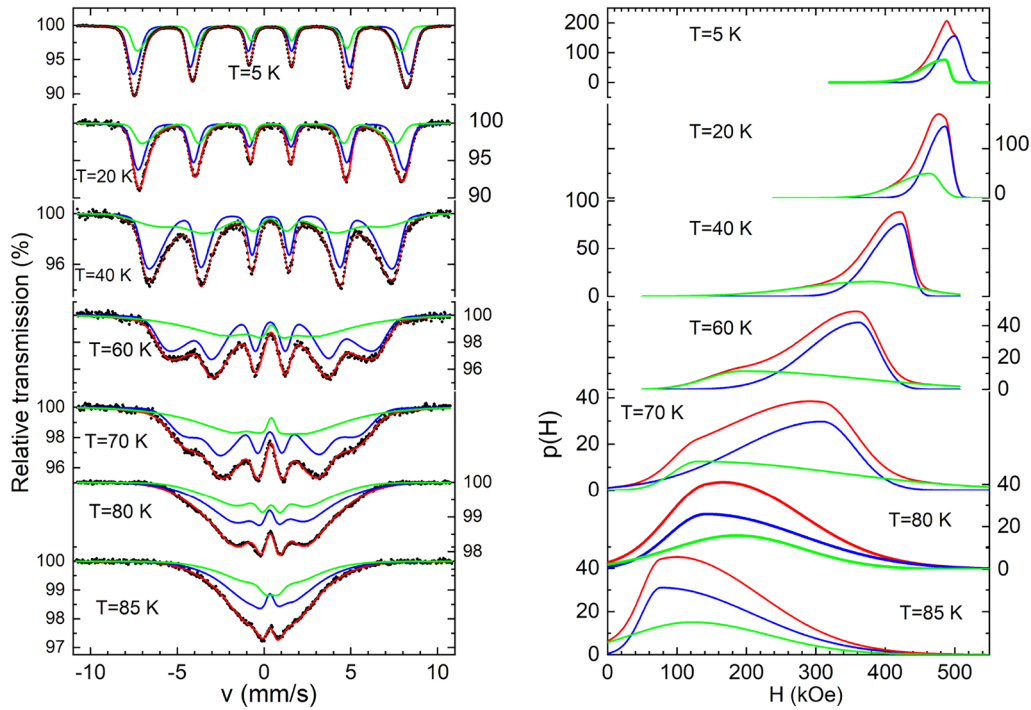
Figure 5: (left panel) Magnetically split MS of α-LiFeO$_2$ phase, fitted with two sextets, supposing an asymmetric Gaussian distribution of the effective hyperfine magnetic field and a symmetric distribution of the quadrupole parameter. The line positions were calculated with the first-order perturbation approximation for the quadrupole interaction. (right panel) Distributions of the hyperfine magnetic field extracted from the fitting of the MS, using a two-sites model.

calculated from the parameters we obtained from the fitting process. The hyperfine parameters obtained from fitting of the MS at $T = 4.2$ K are: $\Gamma_1/2 = \Gamma_2/2 = 0.14$ mm/s (fixed for both sites), $\delta_1 = \delta_2 = 0.482(1)$ mm/s, (are constrained to be equal) $H_1 = 500(1)$ kOe, $u_1 = 0.035(1)$ mm/s, $\sigma_{u,1} = 0.125$ mm/s (fixed), $\sigma_{l,1} = 20(1)$ kOe, $\sigma_{h,1} = 11(1)$ kOe and $A_1 = 63\%$, $H_2 = 487(1)$ kOe, $u_2 = -0.0565(2)$ mm/s, $\sigma_{u,2} = 0.125$ mm/s (fixed), $\sigma_{l,2} = 33(1)$ kOe, $\sigma_{h,2} = 6(1)$ kOe and $A_2 = 37\%$.

The upper panel of Fig. 6 show the temperature evolution of the peaks of the hyperfine magnetic fields distributions for the two sextets. The middle panel of Fig. 6 illustrates the temperature variation of the dc-magnetic susceptibility, $\chi_{dc}(T)$, as measured using the standard zero-field-cooling (ZFC) and field-cooling (FC) protocols under an external magnetic field of 1 kOe. A distinct difference between the ZFC and FC branches is evident below the temperature at which the MS exhibits magnetic splitting. This behavior has been observed in numerous systems with magnetic disorder, where the peak in the ZFC branch of $\chi_{dc}(T)$ has been attributed to a magnetic glass transition [39].

Figure 6 (lower panel) shows the temperature variation of the experimental isomer shift, obtained from the MS fitting, using a two-site model. From the temperature variation of isomer shift, the Debye temperature can be obtained. The isomer shift, δ can be written [38] as the sum of the chemical isomer shift, δ_C (which is

practically temperature independent) and second-order Doppler shift, δ_{SOS} (temperature dependent), $\delta = \delta_C + \delta_{SOS}$.

The second-order Doppler shift is given (in velocity units) by the formula $\delta_{SOD}(T) = -\langle v^2 \rangle/(2c)$, where $\langle v^2 \rangle$ represents the mean square velocity of the Mössbauer atom, and c stands for the speed of light. When considering a Debye phonon spectrum, then (see Shenoy [40]):

$$\langle v^2 \rangle = \frac{9k_B\Theta_D}{8M} + \frac{9k_BT}{M}\left(\frac{T}{\Theta_D}\right)^3 \int_0^{\Theta_D/T} \frac{x^3}{\exp x - 1}dx, \quad (3)$$

where k_B represents the Boltzmann constant, M stands for the mass of the ^{57}Fe isotope, Θ_D denotes the Debye temperature, and T indicates the absolute temperature. Based on experimental data, $\delta_C + \delta_{SOS}(0)$ is estimated to be approximately 0.49 mm/s. In Fig. 6 (lower panel), the solid lines depict theoretical $\delta(T) = \delta_C + \delta_{SOS}(T)$ curves calculated numerically using the Debye model, for Debye temperatures ranging from 400 K to 600 K in increments of 50 K. The curve that closely passes through the experimental data corresponds to a Debye temperature of $\Theta_D = 550 \pm 50$ K.

Heat capacity measurements of α LiFeO$_2$

The upper and middle panels of Fig. 7 depict the temperature variation of the heat capacity under constant pressure C_p and the
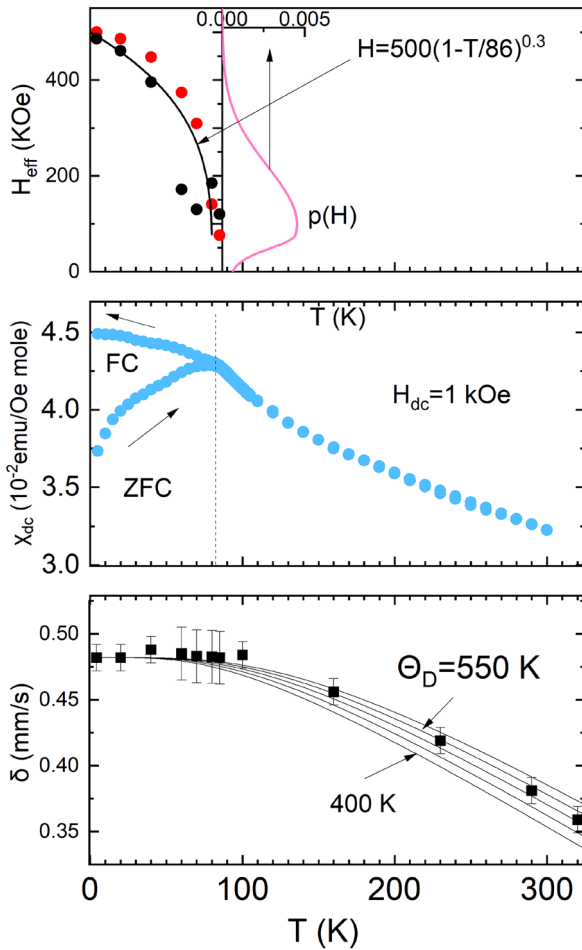
Figure 6: (upper panel) Temperature variation of the peak of the hyperfine magnetic field distributions for the two sextets, derived from least-squares fitting of the magnetically split Mössbauer spectra. The solid line with pink color represents the $p(H)$ distribution at $T = 85$ K. (middle panel) Temperature variation of the dc-magnetic susceptibility, measured in zero-field-cooling and field-cooling protocols under an external magnetic field 1 kOe. (lower panel) Temperature variation of the experimental isomer shift (solid circles) of the α-LiFeO$_2$ phase. The solid lines are calculated by using the equation $\delta(T) = \delta_C + \delta_{SOS}(T)$, with $\Theta_D = 400 - 600$ K.

ratio C_p/T of the α-LiFeO$_2$ phase, respectively. Our data exhibit good agreement with those (80 K $\leq T \leq$ 300 K) of King [41]. The higher-temperature region of $C_p \approx 40$ J mol^{-1}K^{-1} remains beneath the Dulong-Petit limit, $C_{DP} \approx 3(n = 2)R \approx 49.4$ J mol^{-1}K^{-1}, where $R = 8.314$ J mol^{-1}K^{-1} is the gas constant and $n = 2$ signifies the number of atoms per formula unit Li$_{0.5}$Fe$_{0.5}$O [42]. This finding suggests that the Debye temperature significantly exceeds 300 K. Unlike the clear peak observed in the ZFC branch of the $\chi_{dc}(T)$ curve (see middle panel of Fig. 6), the specific heat does not display any anomaly as expected for a paramagnetic-antiferromagnetic phase transition. The absence of a lambda-like peak in the specific heat suggests a broad distribution of Néel's temperatures due to numerous configurations
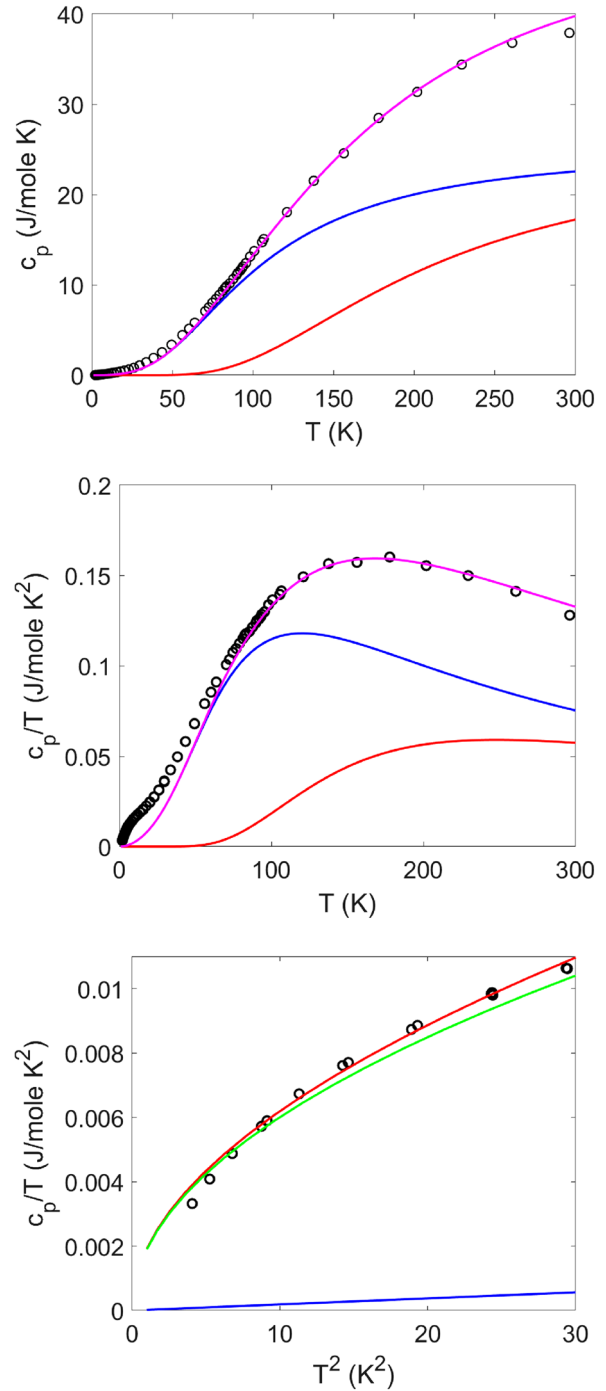

Figure 7: (upper panel) Temperature variation of the experimental heat capacity of the α-LiFeO$_2$ phase, measured under constant pressure. The solid lines represent the theoretical specific heat (magenta line) resulting from the superposition of three isotropic acoustic modes (blue line, $\Theta_D = 430$ K, "Debye contribution") and three optical modes (red line, $\Theta_{E1} = 550$ K, $\Theta_{E2} = \Theta_{E3} = 690$ K, "Einstein contribution"). (middle panel) The same data set as presented in panel (a), but plotted as C_p/T versus T. (lower panel) Variation of C_p/T with T^2 at low temperatures. The red colored line represents the curve $C_p = B_2T^2 + B_3T^3$ (refer to the main text).

existing in a mixed crystal, where in addition, one of the two atoms is diamagnetic. A wide Néel temperature distribution effectively blurs the anticipated lambda-type magnetic transition in the specific heat data. The broad distribution of the effective hyperfine magnetic field (starting from zero magnetic field), observed within the temperature range of [70 K, 85 K], further supports this explanation for the absence of a lambda-type magnetic transition.

Over a broad temperature range, the phonon component of the specific heat can be effectively described using a hybrid Debye-Einstein model (as outlined in [43], p. 77).

$$C_{DE} = 9R\left(\frac{T}{\Theta_D}\right)^3 \int_0^{\Theta_D/T} \frac{x^4 e^x}{(e^x-1)^2}dx + \\ + 3R\sum_{i=1}^{3} \frac{(\Theta_{E,i}/T)^2 e^{\Theta_{E,i}/T}}{(e^{\Theta_{E,i}/T}-1)} \quad (4)$$

The first term represents the specific heat contribution from three degenerate acoustic phonons. The second term approximates the contribution of optical phonons using three Einstein modes with Einstein temperatures $\Theta_{E1} = 550$ K and $\Theta_{E2} = \Theta_{E3} = 690$ K. The Debye, Einstein contributions and their sum are depicted with solid lines in the upper and middle panels of Fig. 7. The additional specific heat relative to the total, occurring below 90 K, is probably related to the contribution of the disordered magnetic state. The lower panel of Fig. 7 displays the low-temperature variation of the C_p/T as a function of T^2. The experimental data can be reproduced with cubic and quadratic temperature terms $C_p = B_2 T^2 + B_3 T^3$, with $B_2 = 1.91^{-3}$ J mol^{-1}K^{-3} and $B_3 = 1.872 \times 10^{-5}$ J mol^{-1}K^{-4}. The low-temperature specific heat for a magnetic insulator can be approximated by the relation [44]

$$C_p = C_{ph} + C_{sw}.$$

The first term $C_{ph} = B_3 T^3$, represents the acoustic phonons contribution to the specific heat with $B_3 = (12\pi^4 nR/5\Theta_D^3)$. $n = 2$ is the number of atoms per chemical formula [42] and Θ_D is the Debye temperature. From the B_3 constant considering three degenerate acoustic modes, we deduce a Debye temperature $\Theta_D = 470$ K. The conventional Debye temperature for four atoms per molecule (e.g. LiFeO$_2$) is $2^{1/3}\Theta_D = 592$ K. This value agrees with the one we estimated from the temperature dependence of the isomer shift. The second term is possibly related to magnon excitations. Kubo [45] predicted a quadratic low-temperature variation of the specific heat for a 2D Heisenberg antiferromagnet in the temperature interval $E_a < k_B T < k_B T_N$, where E_a represents the magnetic anisotropy energy in the spin wave spectrum.

It is helpful to compare our specific heat data with those of LiCoO$_2$ [46, 47]. The existence, in effect, of only one cubic term in low-temperature data [47] has been explained as a signature

of the fully stoichiometric LiCoO$_2$. From the low-temperature cubic term a Debye temperature $\Theta_D = 834 \pm 28$ K (or $834(2/4)^{1/3} = 589$ K for a Li$_{0.5}$Co$_{0.5}$O formula unit) is estimated. This value is higher that deduced for Li$_{0.5}$Fe$_{0.5}$O compound.

γ-LiFeO$_2$ phase

Figure 8 illustrates the MS of γ-LiFeO$_2$ phase from $T = 4.2$ K up to 312 K. In the same figure, we plotted the distributions of the effective hyperfine magnetic field, estimated with the Le Caer–Dubois method. We found that the Le Caer–Dubois method is the best strategy to fit the spectra, yielding effective magnetic field distributions across the full range of temperatures. In this code [37], the absorption line positions are calculated from the first-order perturbation approximation, $\nu_i = \gamma_i H + \delta + \beta_i u$ (see "α-LiFeO$_2$" section for the meaning of symbols). Since this code does not fit the isomer shift δ, the quadrupole shift parameter u, and the HWHM parameter $\Gamma/2$, we estimated these parameters by a trial and error procedure to minimize the χ^2. We used a single value for the quadrupole shift parameter for all temperatures, $u = -0.115$ mm/s. If we take into account that the principal axis of the EFG tensor is parallel to the tetragonal crystallographic c-axis ($\theta = 0$) and the asymmetry parameter is $\eta = 0$ (due to the tetragonal symmetry), we can estimate the quadrupole coupling constant $e^2 q_{zz}Q/2 = 2u = -0.24$ mm/s. The value of the quadrupole coupling constant estimated in the present study agrees very well with the one reported in the earlier study of Cox et al. [4]. Because e and Q are positive constants, the V_{zz} is a negative number. For reference, we quote the hyperfine parameters used to estimate the distribution of the effective magnetic field at $T = 4.2$ K, $\Gamma/2 = 0.15$ mm/s (fixed), $u = -0.115$ mm/s (deduced by trial and error), $\delta = 0.546$ mm/s (deduced by trial and error). From the estimated magnetic field distribution, a mean value of $\langle H \rangle = 525$ kOe with standard deviation 8 kOe was calculated. The isomer shift, the u, and $\langle H \rangle$ values are in good agreement with those found by Tabuchi et al. [18], at $T = 4.2$ K in a γ-LiFeO$_2$ sample prepared hydrothermally.

The estimated isomer shift is plotted as a function of temperature in the lower panel of Fig. 9. Utilizing the same procedure as in the case of α-LiFeO$_2$, we deduce a Debye temperature of $\Theta_D = 300 \pm 50$ K for the γ-LiFeO$_2$ sample. An important question arises: What is the physical explanation for a distribution of hyperfine magnetic fields in the MS? Ideally, only one sextet should exist, as only one crystallographic site within that particular crystal structure exists. A reasonable answer to this question could be based on the fact that a small percentage of iron occupies the Li site and vice versa. According to the results of the Rietveld analysis, this proportion amounts to a maximum of 2%. However, in our spectra, the proportion of the second sextet is approximately 16%, which is significantly greater than the

Figure 8: (left panels) Mössbauer spectra of γ-LiFeO$_2$ with estimated effective magnetic field distributions (right panels) using the Le Caer–Dubois method at several temperatures.
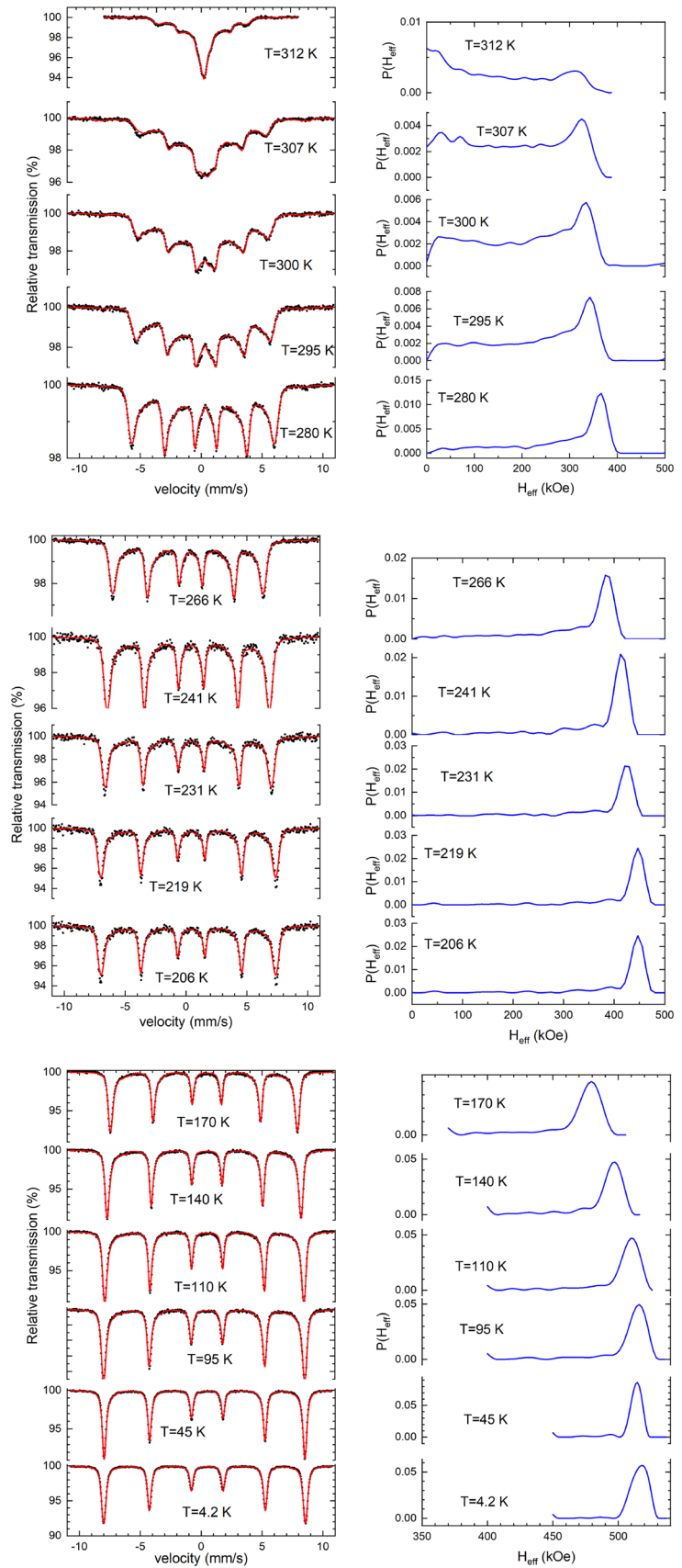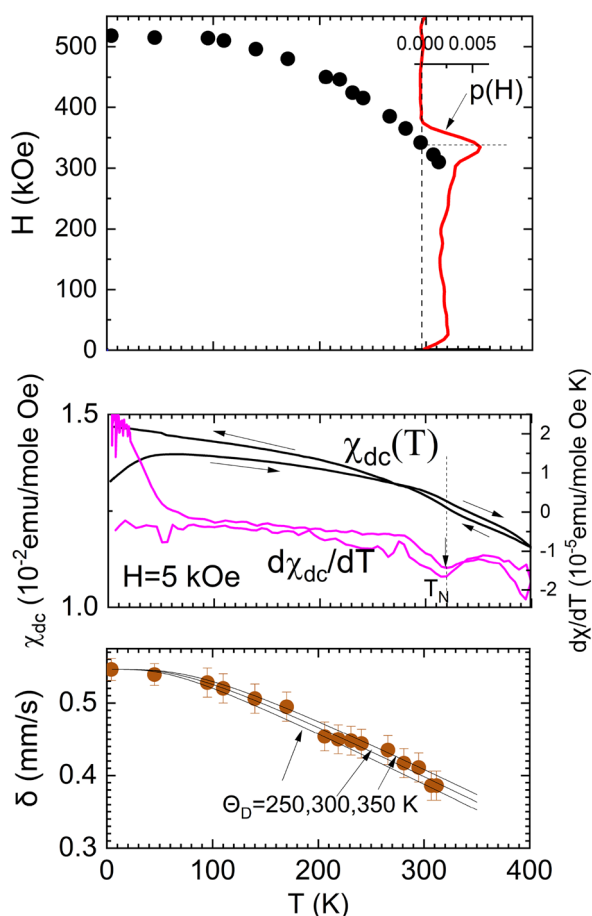
Figure 9: Mössbauer and magnetic data of γ-LiFeO$_2$ compound. (upper panel) Local maxima of the effective hyperfine magnetic field distributions versus temperature estimated from Mössbauer spectra. The solid line represents the $p(H)$ distribution at $T = 295$ K. (middle panel) Temperature variation of the dc-magnetic susceptibility, $\chi_{dc}(T)$, and $d\chi_{dc}(T)/dT$. The measurements are collected in ZFC and FC modes under a dc magnetic field of 5kOe. (lower panel) Temperature variation of experimental and theoretical calculated isomer shift using calculated from second-order Doppler shift. The curves represent $\delta(T)$ curves for $\Theta_D = 250$, 300, and 350 K.

Rietveld estimate. This leads us to speculate that the distribution may arise from iron at the boundaries of coherent Li:Fe ordered regions. The size of the coherently diffracting domains, deduced from the selective broadening of Bragg peaks that describe the Li/Fe ordering in the γ-phase, was estimated to be around 54 nm, or equivalently, about 62 cells. Since each cell contains four iron ions, the total count of Fe ions, denoted as N_{Fe}, would be $62 \times 4 = 248$ Fe ions. If we also assume that the boundaries of the scattering regions align with a specific number of unit cells, for instance, 5 cells, then the disordered iron ions would amount to $5 \times 4 = 20$, which corresponds to $20/248 = 8\%$ of the total. Thus, it is reasonable to suggest that a significant second component may arise from iron ions located at the boundaries of the coherently scattering regions, also known as antiphase

boundaries. As the temperature rises, the overall splitting of the MS diminishes. This implies that the most probable value of H declines monotonically, as depicted in the upper panel of Fig. 9. Moreover, the distribution of hyperfine magnetic fields widens with increasing temperature. Around $T = 300$ K, this distribution becomes quite broad, reaching its peak at the most probable value and extending to zero field. These findings reveal a pronounced disordering of the magnetic state.

The magnetic dc-susceptibility of this sample, measured under a DC-magnetic field of $H = 5$ kOe using both ZFC and FC protocols, (see middle panel of Fig. 9) exhibits slight hysteresis between the ZFC and FC branches within the temperature range of 4.2–260 K. However, it does not display a clear signature of a transition from the antiferromagnetic to the paramagnetic state. Only when plotting the first-order derivative ($d\chi_{dc}/dT$, as shown in the middle panel of Fig. 9) can one identify an anomaly at approximately $T \approx 320$ K. The corresponding MS at $T = 312$ K can be fitted with a highly broad distribution of the hyperfine field, featuring two peaks: one at around ≈ 310 kOe and a second close to zero field at ≈ 25 kOe (refer to Fig. 8, right column).

Nominally β' LiFeO$_2$ sample

The MS of the nominally β'-LiFeO$_2$ sample, measured at temperatures of 4.2 K, 40 K, 80 K, 150 K, 200 K, and 295 K (see SI, Fig. S4). According to the results of the Rietveld analysis for this specific sample, the MS is expected to contain contributions from the β'-LiFeO$_2$, γ-LiFeO$_2$, and α-LiFeO$_2$ phases. Since in γ phase iron occupies predominately a single crystallographic site, the MS at $T = 4.2$ K should manifest as a single sextet with a distribution of hyperfine fields H (as detailed in "γ-LiFeO$_2$ phase" section). Given that this phase comprises nanoregions, its MS spectrum is expected to be more complex. In the monoclinic β'-phase, iron and lithium ions are distributed into four distinct sites ($4e_i$, where $i = 1, 2, 3$, and 4). Among these, $4e_1$ and $4e_3$ are predominantly occupied by iron, while the other two are occupied by lithium. It is reasonable expectation that the MS at $T = 4.2$ K should be comprised two sextets. A cursory examination of lines 1 and 6 in the MS at $T = 4.2$ K reveals structure within these lines. Drawing from the findings of "γ-LiFeO$_2$ phase" section, the outer regions of lines 1 and 6 can be accurately reproduced by a sextet featuring hyperfine parameters close to those of the γ phase. The remaining spectral area can be mainly associated with the β' phase.

An initial attempt to fit the MS at 4.2 K using three sextets, each with an asymmetric distribution of hyperfine fields, disclosed that a minimum of four sextets are necessary to replicate the experimental spectra. A broadened fourth sextet can be attributed to both the γ phase and the α phase. Employing this model, we consistently simulated the 4.2 K, 40 K, and 80

K Mössbauer spectra. The hyperfine parameters used to reproduce this sextet are: $\delta_1 = 0.56$ mm/s, $H_1 = 520$ kOe, $u_1 = -0.11$ mm/s, $\sigma_{l,1} = 10$ kOe, $\sigma_{h,1} = 5$ kOe and $A_1 = 23\%$. This sextet depicted in blue in Fig. S4 (see SI), can be attributed to the γ phase. The hyperfine parameters of the sextets related with the β' phase are: $\delta_2 = 0.43$ mm/s, $H_2 = 517$ kOe, $u_2 = -0.04$ mm/s, $\sigma_{l,2} = 23$ kOe, $\sigma_{h,2} = 11$ kOe, and $A_2 = 25\%$ and $\delta_3 = 0.51$ mm/s, $H_3 = 473$ kOe, $u_3 = -0.15$ mm/s, $\sigma_{l,3} = 9$ kOe, $\sigma_{h,3} = 16$ kOe and $A_3 = 26\%$ (sextets colored with magenta and brown colors, respectively in Fig S4 (see SI)). The hyperfine parameters of the fourth sextet related to the γ (predominantly) and α phase are: $\delta_4 = 0.51$ mm/s, $H_4 = 482$ kOe, $u_4 = 0.05$ mm/s, $\sigma_{l,4} = 8$ kOe, $\sigma_{h,4} = 9$ kOe, and $A_4 = 26\%$ (shown with green color in Fig. S4 (see SI)). At 140 K, the MS consists of a magnetic sextet characterized by a very broad distribution of H, accompanied by a central unresolved region. At 200 K, the magnetic sextets are still present, albeit with a smaller spectral area in comparison to the 140 K spectrum. The central unresolved spectral region may be attributed to either paramagnetic/fast-relaxing entities or magnetically split sextets with small magnetic fields. At ambient temperature, the MS is composed of an unresolved spectral area resulting from the paramagnetic doublets of the α phase, β' and γ nanoregions. The temperature dependence of the dc-magnetic moment, (see Supplementary information Fig. S5), exhibits significant hysteresis between the ZFC and FC branches, indicating the presence of nanoregions (superparamagnetic behavior) within the sample. The peak observed at 150 K is reasonably attributed to the magnetic transition of the β' phase. The convergence of the ZFC and FC branches observed around 250 K can be attributed to the superparamagnetic behavior of the γ phase nanoregions.

Conclusions

We conducted a study on the crystal structure of the LiFeO$_2$ compound in its three polymorphic forms using powder XRD data and the local magnetic properties through MS and magnetization studies. The primary finding of our investigation on the disordered cubic α-LiFeO$_2$ phase is that the MS exhibit broad spectral lines in both the paramagnetic and antiferromagnetic states. This indicates a distribution of the hyperfine parameters. The paramagnetic spectra can be accurately reproduced with a two-peak distribution of the ΔE_Q parameter, which we estimated using the Le Caer–Dubois method. For the magnetically split MS, we employed a model involving two sextets, convoluted with temperature-dependent asymmetric and temperature-independent symmetric distributions of the effective magnetic field $p_i(H)$ ($i = 1, 2$) and the quadrupole parameter $p_i(u)$, respectively. The broad, temperature-dependent distributions $p_i(H)$ calculated from MS indicate a wide distribution of the Néel temperature or spin glass behavior. This behavior is inherent to

the disorder and the short-range ordering present in this mixed crystal.

The γ-LiFeO$_2$ phase was prepared through prolonged annealing of the α-LiFeO$_2$ below the order–disorder transition temperature. Despite the extended annealing, Rietveld analysis indicates a selective broadening of the reflections with $\ell = 2n + 1$. This broadening likely originates from antiphase domains. These defects significantly influence the magnetically split MS from low temperatures up to the Néel temperature. We calculated the effective hyperfine magnetic field distributions ($p(H)$) using the Le Caer–Dubois method. The temperature dependence of these distributions, particularly below the magnetic transition temperature, is linked to a broad distribution of the Néel temperature due to the presence of the antiphase defects. The hyperfine parameters extracted from the MS indicate that iron predominantly exists in a high spin ferric state.

Efforts to synthesize the β'-LiFeO$_2$ phase as a single-phase sample proved unsuccessful. Rietveld analysis of the XRD data of these samples revealed that they consist of nanoregions containing both β'-LiFeO$_2$ and γ-LiFeO$_2$ phases. According to the MS and magnetic measurements, the β'-LiFeO$_2$ phase exhibits a magnetic transition at 150 K.

Methods and experimental details

α-LiFeO$_2$ polycrystalline samples are prepared by solid-state reaction of stoichiometric amounts of Li$_2$CO$_3$ and Fe$_2$O$_3$ powders (99.99% and 99.9% purity, respectively). Initially, the Li$_2$CO$_3$ and Fe$_2$O$_3$ powders are thoroughly mixed in an agate mortar and pestle. Subsequently, the mixed powders are pressed (180 kg/cm^2) with a cylindrical die. The cylindrical pastilles were slowly heated to the reaction temperature in an alumina crucible. The reaction temperature is selected in the interval 800–950 °C. The grinding, pastille formation, and reaction process were repeated twice. Finally, the samples were either cooled slowly to ambient temperature or quenched from the reaction temperature into water. The γ-LiFeO$_2$ polycrystalline sample was prepared by annealing a α-LiFeO$_2$ sample for 30 days, at 600°C. We attempted to prepare single phase β'-LiFeO$_2$ by prolonged annealing an α-LiFeO$_2$ in the temperature interval 250–500 °C, but without success (see below).

The magnetic ac-susceptibility, dc-magnetization, and specific heat measurements were carried out with a Physical Property Measurement System (PPMS, Quantum Design) using the ACMS and specific heat options and with a SQUID magnetometer (Quantum Design MPMS 5.5). Absorption Mössbauer spectra (MS) were measured using a conventional constant acceleration spectrometer with a ^{57}Co(Rh) source oscillating at room temperature. The spectrometer was calibrated with a thin α-Fe foil at ambient conditions. Isomer shifts are referred to α-Fe at 295 K. The powder X-ray diffraction patterns of the polycrystalline samples

were measured in the Bragg–Brentano geometry using Siemens/Bruker D5000 and smartlab Rigaku diffractometers, both operated at 40 kV and 35 mA, with CuK$_\alpha$ radiation ($\lambda_1 = 1.54184$Å). The powder XRD patterns were analyzed with the Rietveld method using the FULLPROF program suite [34, 48]. Thermogravimetric measurements were performed with a Perkin-Elmer (Pyris Diamond TG/TDA) apparatus.

Author contributions

All authors contribute equally.

Funding

Data availability

The data are available from V.P. or M.P. upon request.

Declarations

Conflict of interest The authors declare they have no Conflict of interest statement/Conflict of interest.

Ethical approval

Not applicable.

Consent to participate

Informed consent was obtained from all individual participants included in the study.

Consent for publication

Informed consent was obtained from all individual participants included in the study.

Supplementary Information

The online version contains supplementary material available at https://doi.org/10.1557/s43578-024-01338-0.

Open Access

References

1. T. Hewston, B. Chamberland, A survey of first-row ternary oxides LiMO$_2$ (M=Sc-Cu). J. Phys. Chem. Solids **48**, 97 (1987). https://doi.org/10.1016/0022-3697(87)90076-X
2. R. Collongues, C. R. Acad. Sci. **241**, 1577 (1955)
3. M. Fayard, Ann. Chim. Fr. **6**, 1279 (1961)
4. D.E. Cox, G. Shirane, P.A. Flinn, S.L. Ruby, W.J. Takei, Neutron diffraction and mössbauer study of ordered and disordered LiFeO$_2$. Phys. Rev. **132**, 1547 (1963). https://doi.org/10.1103/PhysRev.132.1547
5. J. Anderson, M. Schieber, Order-disorder transitions in heat-treated rock-salt lithium ferrite. J. Phys. Chem. Solids **25**, 961 (1964). https://doi.org/10.1016/0022-3697(64)90033-2
6. M. Brunel, F. de Bergevin, Ordre a courte distance, deplacements locaux des ions et energie electrostatique dans FeLiO$_2$. J. Phys. Chem. Solids **30**, 2011 (1969). https://doi.org/10.1016/0022-3697(69)90180-2
7. M. Brunel, F. De Bergevin, M. Gondrand, Determination theorique et domaines d'existence des differentes surstructures dans les composes A^{3+} B^{1+} X$_2^{2-}$ de type NaCl. J. Phys. Chem. Solids **33**, 1927 (1972). https://doi.org/10.1016/S0022-3697(72)80492-X
8. R. Famery, P. Bassoul, F. Queyroux, Structure and morphology study of the metastable Q2 form in LiFeO$_2$ ferrite by X-ray diffraction and transmission electron microscopy. J. Solid State Chem. **57**, 178 (1985). https://doi.org/10.1016/S0022-4596(85)80007-4
9. R. Famery, P. Bassoul, F. Queyroux, Morphology and twinning study of the ordered Q1 form in LiFeO$_2$ ferrite. J. Solid State Chem. **61**, 293 (1986). https://doi.org/10.1016/0022-4596(86)90034-4
10. C. Julien, F. Gendron, A. Amdouni, M. Massot, Lattice vibrations of materials for lithium rechargeable batteries. VI. Ordered spinels. Mater. Sci. Eng. **130**, 41 (2006). https://doi.org/10.1016/j.mseb.2006.02.003
11. S. Layek, E. Greenberg, W. Xu, G.K. Rozenberg, M.P. Pasternak, J.-P. Itié, D.G. Merkel, Pressure-induced spin crossover in

disordered LiFeO$_2$. Phys. Rev. B **94**, 125129 (2016). https://doi.org/10.1103/PhysRevB.94.125129

12. M. Rahman, J.-Z. Wang, M.F. Hassan, Z. Chen, H.-K. Liu, Synthesis of carbon coated nanocrystalline porous α-LiFeO$_2$ composite and its application as anode for the lithium ion battery. J. Alloy Compd. **509**, 5408 (2011). https://doi.org/10.1016/j.jallcom.2011.02.067

13. P. Rosaiah, O.M. Hussain, Synthesis, electrical and dielectrical properties of lithium iron oxide. Adv. Mater. Lett. **4**, 288 (2013)

14. J.G. Allpress, Electron microscopy of lithium ferrites. precipitation of LiFe$_5$ O$_8$ in α-LiFeO$_2$. J. Mater. Sci. **6**, 313–318 (1971). https://doi.org/10.1007/BF02403098

15. J.M. Cowley, High-resolution dark-field electron microscopy. II. Short-range order in crystals. Acta Crystallogr. Sect. A **29**, 537 (1973). https://doi.org/10.1107/S0567739473001336

16. M. Mitome, S. Kohiki, Y. Murakawa, K. Hori, K. Kurashima, Y. Bando, Transmission electron microscopy and electron diffraction study of the short-range ordering structure of α-LiFeO$_2$. Acta Crystallogr. B **60**, 698 (2004). https://doi.org/10.1107/S0108768104023456

17. O. Knop, C. Ayasse, J. Carlow, W. Barker, F. Woodhams, R. Meads, W. Parker, Origin of the quadrupole splitting in the mössbauer ^{57} Fe spectrum of cubic (disordered) LiFeO$_2$. J. Solid State Chem. **25**, 329 (1978). https://doi.org/10.1016/0022-4596(78)90119-6

18. M. Tabuchi, S. Tsutsui, C. Masquelier, R. Kanno, K. Ado, I. Matsubara, S. Nasu, H. Kageyama, Effect of cation arrangement on the magnetic properties of lithium ferrites (LiFeO$_2$) prepared by hydrothermal reaction and post-annealing method. J. Solid State Chem. **140**, 159 (1998). https://doi.org/10.1006/jssc.1998.7725

19. F. Du, X. Bie, H. Ehrenberg, L. Liu, C. Gao, Y. Wei, G. Chen, H. Chen, C. Wang, Unusual magnetism due to a random distribution of cations in α-LiFeO$_2$. J. Phys. Soc. Jpn. **80**, 094705 (2011). https://doi.org/10.1143/JPSJ.80.094705

20. R. De Ridder, D. Van Dyck, G. Van Tendeloo, S. Amelinckx, A cluster model for the transition state and its study by means of electron diffraction. Application to some particular systems. Physica Status Solidi (a) **40**, 669 (1977). https://doi.org/10.1002/pssa.2210400235

21. M. Barré, M. Catti, Neutron diffraction study of the β' and γ phases of LiFeO$_2$. J. Solid State Chem. **182**, 2549 (2009). https://doi.org/10.1016/j.jssc.2009.06.029

22. M. Tabuchi, K. Ado, H. Sakaebe, C. Masquelier, H. Kageyama, Preparation of AFeO$_2$ (A=Li, Na) by hydrothermal method. Solid State Ionics **79**, 220 (1995). https://doi.org/10.1016/0167-2738(95)00065-E

23. M. Brunel, F. de Bergevin, Structure de la phase QII (ou β) du ferrite de lithium FeLiO$_2$: Exemple d'antiphase periodique. J. Phys. Chem. Solids **29**, 163 (1968). https://doi.org/10.1016/0022-3697(68)90266-7

24. Y. Hu, H. Zhao, X. Liu, A simple, quick and eco-friendly strategy of synthesis nanosized α-LiFeO$_2$ cathode with excellent electrochemical performance for lithium-ion batteries. Materials **11**, 1176 (2018). https://doi.org/10.3390/ma11071176

25. Z. jia Zhang, J.-Z. Wang, S.-L. Chou, H.-K. Liu, K. Ozawa, H. jun Li, Polypyrrole-coated α-LiFeO$_2$ nanocomposite with enhanced electrochemical properties for lithium-ion batteries. Electrochim. Acta **108**, 820 (2013). https://doi.org/10.1016/j.electacta.2013.06.130

26. J. Morales, J. Santos-Peña, Highly electroactive nanosized α-LiFeO$_2$. Electrochem. Commun. **9**, 2116 (2007). https://doi.org/10.1016/j.elecom.2007.06.013

27. P.P. Prosini, M. Carewska, S. Loreti, C. Minarini, S. Passerini, Lithium iron oxide as alternative anode for Li-ion batteries. Int. J. Inorg. Mater. **2**, 365 (2000). https://doi.org/10.1016/S1466-6049(00)00028-3

28. J. Morales, J. Santos-Peña, R. Trócoli, S. Franger, E. Rodríguez-Castellón, Insights into the electrochemical activity of nanosized α-LiFeO$_2$. Electrochim. Acta **53**, 6366 (2008). https://doi.org/10.1016/j.electacta.2008.04.057

29. M. Hirayama, H. Tomita, K. Kubota, H. Ido, R. Kanno, Synthesis and electrochemical properties of nanosized LiFeO$_2$ particles with a layered rocksalt structure for lithium batteries. Mater. Res. Bull. **47**, 79 (2012). https://doi.org/10.1016/j.materresbull.2011.09.024

30. Y. Lee, S. Sato, Y. Sun, K. Kobayakawa, Y. Sato, A new type of orthorhombic LiFeO$_2$ with advanced battery performance and its structural change during cycling. J. Power Sources **119–121**, 285 (2003). https://doi.org/10.1016/S0378-7753(03)00152-6

31. S.-H. Wu, H.-Y. Liu, Preparation of α-LiFeO$_2$-based cathode materials by an ionic exchange method. J. Power Sources **174**, 789 (2007). https://doi.org/10.1016/j.jpowsour.2007.06.230

32. P. Suresh, A. Shukla, N. Munichandraiah, Synthesis and characterization of LiFeO$_2$ and LiFe$_{0.9}$ Co$_{0.1}$ O$_2$ as cathode materials for Li-ion cells. J. Power Sources **159**, 1395 (2006). https://doi.org/10.1016/j.jpowsour.2005.12.034

33. S.-P. Guo, Z. Ma, J.-C. Li, H.-G. Xue, Facile preparation and promising lithium storage ability of α-LiFeO$_2$/porous carbon nanocomposite. J. Alloy Compd. **711**, 8 (2017). https://doi.org/10.1016/j.jallcom.2017.03.332

34. J. Rodríguez-Carvajal, Recent advances in magnetic structure determination by neutron powder diffraction. Physica B **192**, 55 (1993). https://doi.org/10.1016/0921-4526(93)90108-I

35. G. Williamson, W. Hall, X-ray line broadening from filed aluminium and wolfram. Acta Metall. **1**, 22 (1953). https://doi.org/10.1016/0001-6160(53)90006-6

36. According to fullprof user guide: strains are given in %%($\times 10^4$), ($\epsilon = 1/2\beta^* d$). The strain here correspond to 1/4 of the apparent strain defined by Stokes and Wilson. It is the so-called Maximum strain and related by a constant factor to the

root-mean-square-strain (RMSS). In case of Gaussian distribution $\epsilon(\text{RMS}) = \sqrt{2/\pi}\,\epsilon$

37. G.L. Caer, J.M. Dubois, Evaluation of hyperfine parameter distributions from overlapped mossbauer spectra of amorphous alloys. J. Phys. E **12**, 1083 (1979). https://doi.org/10.1088/0022-3735/12/11/018

38. P. Gütlich, E. Bill, A.X. Trautwein, *Mössbauer Spectroscopy and Transition Metal Chemistry Fundamentals and Applications* (Springer, New York, 2011). https://doi.org/10.1007/978-3-540-88428-6

39. K. Binder, A.P. Young, Spin glasses: experimental facts, theoretical concepts, and open questions. Rev. Mod. Phys. **58**, 801 (1986). https://doi.org/10.1103/RevModPhys.58.801

40. G.K. Shenoy, Mössbauer Isomer. Shifts, ed. by G.K. Shenoy, F.E. Wagner (North-Holland, Amsterdam, 1978)

41. E.G. King, J. Am. Chem. Soc. **77**, 3189–3190 (1955). https://doi.org/10.1021/ja01617a007

42. In the analysis of the specific heat data we consider that the asymmetry unit is $Li_{0.5}Fe_{0.5}O$ so it contains $n = 2$ atoms

43. M. Born, *Dynamik der Kristallgitter* (Druck und Verlag, von B. G. Teubner, 1915)

44. E.S.R. Gopal, *Specific Heats at Low Temperatures* (Plenum, New York, 1966)

45. R. Kubo, The spin-wave theory of antiferromagnetics. Phys. Rev. **87**, 568 (1952). https://doi.org/10.1103/PhysRev.87.568

46. J.T. Hertz, Q. Huang, T. McQueen, T. Klimczuk, J.W.G. Bos, L. Viciu, R.J. Cava, Phys. Rev. B **77**, 075119 (2008). https://doi.org/10.1103/PhysRevB.77.075119

47. M. Meńetrier, D. Carlier, M. Blangero, C. Delmas, On really stoichiometric $LiCoO_2$. Electrochem. Solid-State Lett. **11**, A179 (2008). https://doi.org/10.1149/1.2968953

48. T. Roisnel, J. Rodríquez-Carvajal, Winplotr: a windows tool for powder diffraction patterns analysis. Mater. Science Forum **378–381**, 118 (2001). https://doi.org/10.4028/www.scientific.net/msf.378-381.118